

# The dust scattering halo of Cygnus X-3

L. R. Corrales<sup>1,2★</sup> and F. Paerels<sup>2,3★</sup>

<sup>1</sup>MIT Kavli Institute for Astrophysics and Space Research, 77 Massachusetts Ave, 37-241, Cambridge, MA 02139, USA

<sup>2</sup>Columbia University, Mail Code 5246, 550 West 120th Street, New York, NY 10027, USA

<sup>3</sup>Columbia Astrophysics Laboratory, Mail Code 5247, 550 West 120th Street, New York, NY 10027, USA

Accepted 2015 July 24. Received 2015 July 21; in original form 2015 May 28

## ABSTRACT

Dust grains scatter X-ray light through small angles, producing a diffuse halo image around bright X-ray point sources situated behind a large amount of interstellar material. We present analytic solutions to the integral for the dust scattering intensity, which allow for a Bayesian analysis of the scattering halo around Cygnus X-3. Fitting the optically thin 4–6 keV halo surface brightness profile yields the dust grain size and spatial distribution. We assume a power-law distribution of grain sizes ( $n \propto a^{-p}$ ) and fit for  $p$ , the grain radius cut-off  $a_{\max}$ , and dust mass column. We find that a  $p \approx 3.5$  dust grain size distribution with  $a_{\max} \approx 0.2 \mu\text{m}$  fits the halo profile relatively well, whether the dust is distributed uniformly along the line of sight or in clumps. We find that a model consisting of two dust screens, representative of foreground spiral arms, requires the foreground Perseus arm to contain 80 per cent of the total dust mass. The remaining 20 per cent of the dust, which may be associated with the outer spiral arm of the Milky Way, is located within 1 kpc of Cyg X-3. Regardless of which model was used, we found  $\tau_{\text{sca}} \sim 2 E_{\text{keV}}^{-2}$ . We examine the energy resolved haloes of Cyg X-3 from 1 to 6 keV and find that there is a sharp drop in scattering halo intensity when  $E < 2\text{--}3$  keV, which cannot be explained with multiple scattering effects. We hypothesize that this may be caused by large dust grains or material with unique dielectric properties, causing the scattering cross-section to depart from the Rayleigh–Gans approximation that is used most often in X-ray scattering studies. The foreground Cyg OB2 association, which contains several evolved stars with large extinction values, is a likely culprit for grains of unique size or composition.

**Key words:** scattering – methods: observational – dust, extinction – ISM: structure – X-rays: individual: Cygnus X-3 – X-rays: ISM.

## 1 INTRODUCTION

Dust grains are a vital part of the interstellar medium (ISM), aiding in gas cooling for star formation, providing a site for chemical reactions, and acting as the seeds for planetesimal growth. ISM dust is typically observed in absorption, over the UV and optical, or emission in the infrared. However, high-energy studies of interstellar dust grains complement information at other wavelengths for several reasons. First, the dust scattering cross-section in the X-ray is highly sensitive to grain radius ( $a$ ), making it ideal for gauging the large end of the size distribution. This is more difficult to do at other wavelengths. Large grains  $\sim 0.3 \mu\text{m}$  in radius have a flat extinction efficiency for UV and optical light, which affects the normalization of the extinction curve and not its slope. Infrared emission ( $\lambda \lesssim 50 \mu\text{m}$ ) also tends to be dominated by the smallest carbonaceous grains (polycyclic aromatic hydrocarbons – PAHs); the larger  $0.1 \mu\text{m}$  grains will glow at these wavelengths only when

subjected to intense radiation (Draine & Li 2007). Secondly, dust grains are relatively transparent to X-rays (Wilms, Allen & McCray 2000). As a consequence, X-rays probe the full abundance of interstellar elements (gas plus dust) and higher ISM column densities than UV or optical studies.

We focus here on dust scattering of X-rays over small angles, which produces a diffuse halo image around bright X-ray point sources (Overbeck 1965). The first X-ray scattering halo was imaged with the Einstein Observatory around 4U1658 – 48 (Rolf 1983). Since then, scattering haloes have been observed around various Galactic X-ray binaries (e.g. Witt, Smith & Dwek 2001; Smith 2008), anomalous X-ray pulsars (Tiengo et al. 2010), and gamma-ray bursts that pass through dusty regions of the Milky Way (Vaughan et al. 2006).

It has been shown that a power-law distribution ( $N_d \propto a^{-p}$  with  $p \approx 3.5$ ) with a mix of graphite and silicate grains reproduce extinction curves in the UV and optical (Mathis, Rumpl & Nordsieck 1977, hereafter MRN). Updated grain size distributions beyond the simple power-law regime have been developed to better reproduce infrared and microwave emission features. Weingartner & Draine (2001,

\* E-mail: lia@space.mit.edu (LRC); frits@astro.columbia.edu (FP)

hereafter WD01) produced a distribution that mainly modified the lower end of the grain size distribution, which shines brightest in the infrared. Zubko, Dwek & Arendt (2004, hereafter ZDA) did the same, but aimed to preserve elemental abundance constraints. They developed a series of models with varying mixtures of silicate, graphite, amorphous carbon, PAH, and composite material sometimes referred to as ‘fluffy’ dust. Several authors have shown that ZDA models fit X-ray scattering haloes comparatively well to slightly better than MRN and WD01 size distributions (Smith et al. 2006; Smith 2008; Valencic et al. 2009). However, the best-fitting ZDA models tended to be BARE-GR and BARE-AC (solid grains of graphite and amorphous carbon), which are more similar to MRN than the ZDA COMP (fluffy grain) models. The goal of this work is to examine how X-ray scattering can help drive our understanding of dust grain size distribution. We take power-law models as a jumping off point, and ask the question: what is the maximum grain size cut-off that can explain X-ray scattering from the diffuse ISM?

We examine one of the brightest X-ray scattering haloes available in the *Chandra* archive, associated with the high-mass X-ray binary (HMXB) Cygnus X-3. We describe the dust scattering physics and foreground ISM environment below. The observation and point spread function (PSF) subtraction method is described in Section 2. We take the Bayesian approach to fitting the dust grain size distribution in Section 3, using two models for the spatial distribution of dust along the line of sight. In one case, we assume dust is uniformly distributed; in the other, we model the halo with two infinitesimally thin dust screens. In Section 4, we present flux measurements and model residuals from energy resolved scattering haloes between 1 and 6 keV. For completeness, we report in Section 5 two alternate fits to the 4–6 keV dust scattering haloes and the model implications for optical and UV extinction. In Section 6, we compare our results to other papers that study ISM on the Cyg X-3 sight line. Conclusions are summarized in Section 7. Finally, the appendix contains the analytic solution for the halo intensity in the case of a power-law distribution of dust grain sizes. These solutions allow for fast computation of the halo surface brightness profile, making Bayesian analysis feasible.

### 1.1 Dust scattering physics

Because Cyg X-3 is situated behind a very large column of gas and dust, it is dark for  $E < 1$  keV. Assuming MRN-type dust, our calculations for the dust scattering cross-section are safely in the Rayleigh-Gans (RG) regime of  $E_{\text{keV}} \gtrsim a_{\mu\text{m}}$ , where  $a$  is the dust grain radius in units of  $\mu\text{m}$  (Smith & Dwek 1998). We follow Smith & Dwek (1998) in applying the Drude approximation for the complex index of refraction, which treats each dust grain as a sphere of free electrons. Assuming that there are on average two baryons in the atomic nucleus for every electron, the total dust scattering cross-section is

$$\sigma_{\text{sca}} \approx 6.2 \times 10^{-7} \rho_3^2 a_{\mu\text{m}}^4 E_{\text{keV}}^{-2} \text{ cm}^2, \quad (1)$$

where  $\rho_3 = \rho/(3 \text{ g cm}^{-3})$ ,  $a_{\mu\text{m}} = a/(1 \mu\text{m})$ , and  $E_{\text{keV}} = E/(1 \text{ keV})$  are typical values.

The RG differential scattering cross-section contains a first-order Bessel function that can be approximated with a Gaussian (Mauche & Gorenstein 1986). Using the Drude approximation again,

$$\frac{d\sigma_{\text{sca}}}{d\Omega} \approx 1.13 \exp\left(\frac{-\theta_{\text{sca}}^2}{2\sigma^2}\right) \rho_3^2 a_{\mu\text{m}}^6 \text{ cm}^2 \text{ ster}^{-1} \quad (2)$$

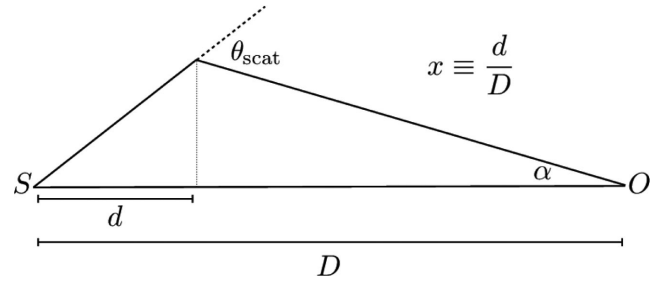


**Figure 1.** Geometry of X-ray scattering through the ISM, with an X-ray point source at  $S$  and observer at  $O$ .

with the characteristic width

$$\tilde{\sigma} = \frac{1.04 \text{ arcmin}}{E_{\text{keV}} a_{\mu\text{m}}}. \quad (3)$$

The intensity of the dust scattering halo is calculated by integrating the scattering cross-section along the line of sight (Fig. 1). A patch of dust grains at  $d \equiv xD$  distance away from the X-ray source at  $S$ ,<sup>1</sup> will see a flux  $L_S/4\pi d^2 = F_a/x^2$  where  $F_a$  is the apparent flux at point  $O$ . Light observed at angle  $\alpha$  requires  $\theta_{\text{sca}} = \alpha/x$ . Using  $N_d$  for the dust column density and  $\xi(x)$  to parametrize the density as a function of position along the line of sight, we get

$$I_h(\alpha, E) = \int_a \int_0^1 \frac{F_a}{x^2} \frac{d\sigma}{d\Omega} \left( \theta_{\text{sca}} = \frac{\alpha}{x} \right) N_d \xi(x) dx da. \quad (4)$$

The dust scattering code used in this work calculates the scattering halo as normalized by apparent source flux,

$$\frac{d\psi_h}{d\Omega}(\alpha, E) = \frac{I_h(\alpha, E)}{F_a} \quad (5)$$

which will be used later in Section 4.

The effect of absorption should be considered carefully because the scattered light takes a longer path (e.g. Trümper & Schönfelder 1973),

$$\delta x = \frac{\alpha^2(1-x)}{2x}. \quad (6)$$

Assuming that the ISM is homogeneous enough that the scattered light path does not differ significantly in extinction properties, dust scattered light is subject to an additional  $\delta\tau_{\text{abs}} \approx \tau_{\text{abs}}\delta x$ , where  $\tau_{\text{abs}}$  is the total absorption along distance  $D$ . By the nature of small angle scattering, the observer at  $O$  will mostly view dust that is at intermediate distances,  $x \sim 1/2$ , making  $\delta x \approx \alpha^2/2$ . The largest observation angles in this study are  $\alpha \sim 100$  arcsec, resulting in  $\delta x \lesssim 10^{-7}$ . This is negligible even for ISM columns where  $N_H \gtrsim 10^{22} \text{ cm}^{-2}$ , which have  $\tau_{\text{abs}} \gtrsim 1$  (Wilms et al. 2000). Thus from here on forward, we combine the absorption term with  $F_a$  so that it represents the absorbed apparent flux as it is incident on the observer:  $F_a \equiv L_S e^{-\tau_{\text{abs}}}/4\pi D^2$ .

We consider two cases: a uniform distribution of dust grains along the line of sight,  $\xi(x) = 1$ , and an infinitesimally thin screen of dust grains at position  $x_s$ , so that  $\xi(x) = \delta(x - x_s)$ .

<sup>1</sup> Note that in other publications involving X-ray scattering,  $x$  is often used to denote the distance between the observer ( $O$ ) and the dust grains. In that case, all instances of  $x$  should be replaced by  $(1-x)$  throughout. We chose to define  $x$  as shown in Fig. 1 for mathematical elegance.

## 1.2 ISM column

Cyg X-3 is located in the galactic plane at  $(l, b) = (79.8, +00.7)$ . At a distance of 7–13 kpc from the Sun (Dickey 1983; Predehl et al. 2000), the HMXB is located behind one or two spiral arms of the Milky Way – Perseus and the outer arm (Russeil 2003; Reid et al. 2014). Cyg X-3 is also situated behind the young stellar association Cyg OB2, which is associated with the larger Cygnus X molecular region (Dame, Hartmann & Thaddeus 2001; Knödlseider 2003; Wright, Drew & Mohr-Smith 2015). This particular sight line thereby offers a unique laboratory for probing dust physics within different ISM phases using the phenomenon of X-ray scattering.

Radio surveys of the 21-cm line give a neutral hydrogen column towards Cyg X-3 of  $N_{\text{H}_1} \gtrsim 10^{22} \text{ cm}^{-2}$  (Kalberla et al. 2005). The Milky Way CO survey shows that the Cyg X-3 sightline is particularly patchy, but contains a total proton density  $N_{\text{H}} \approx 10^{22} \text{ cm}^{-2}$  in the form of molecular hydrogen (Dame et al. 2001). Taking both these measurements as a lower limit, because Cyg X-3 seems to be near the edge of the Galaxy and because we expect some portion of the ISM hydrogen to be ionized, the total ISM column is likely  $N_{\text{H}} > 2 \times 10^{22} \text{ cm}^{-2}$ .

X-ray spectroscopy offers another means to measure the ISM column density. Absorption by neutral hydrogen via the photoelectric effect dominates below 1 keV, but the metal content of the ISM accounts for a considerable fraction of the total absorption above 1 keV (Wilms et al. 2000). Predehl & Schmitt (1995) used *ROSAT* observations of Cyg X-3 to estimate  $N_{\text{H}} \approx 3\text{--}4 \times 10^{22} \text{ cm}^{-2}$ , which is consistent with the above radio surveys. They also estimate the total optical depth to scattering for Cyg X-3 is  $\tau_{\text{sca}} \sim 1.5 E_{\text{keV}}^{-2}$ , which means that the extinctive effects of dust scattering must be incorporated into spectral models for ISM extinction. This is particularly relevant for the high-resolution optics of *Chandra* because scattering removes light from the source extraction region.

## 2 DATA REDUCTION

The 0.5 arcsec pixel $^{-1}$  resolution and low background makes *Chandra* the best X-ray observatory available for imaging dust scattering haloes (Weisskopf et al. 2000). We chose to analyse the longest *Chandra* observation (50 ks) of Cygnus X-3, ObsId 6601, which was taken with the High-Energy Transmission Grating (HETG; Canizares et al. 2005). The data presented in this work was extracted using common data reduction procedures and CIAO version 4.5.

### 2.1 Fit to the HETG spectrum

We used the `tg_findzoo` tool in CIAO to centre the HETG extraction regions on the point source, then used standard calibration methods to get a spectrum of Cyg X-3, shown in Fig. 2. Some disagreement between the MEG and HEG spectrum in the 3–5 keV energy range is an indication of pileup (discussed in more detail in Section 2.2), because light is dispersed over smaller angles with the MEG as compared to the HEG. To test for possible non-linear effects in the HEG arms, we applied the pileup correction `simple_gpil2` (Nowak et al. 2008; Hanke et al. 2009) with the physical spectral models described below. We found that the MEG and HEG arms could be fit simultaneously with less than 1 per cent of HEG counts being affected by pileup. Pileup is complicated by the fact that Cyg X-3 is a variable source (Section 4.4). Based on the raw counts taken from time intervals when Cyg X-3 is at its brightest, which is about 20 per cent of the full exposure time, the HEG spectrum will experience  $\leq 7$  per cent pileup in the region around 4–5 keV. From

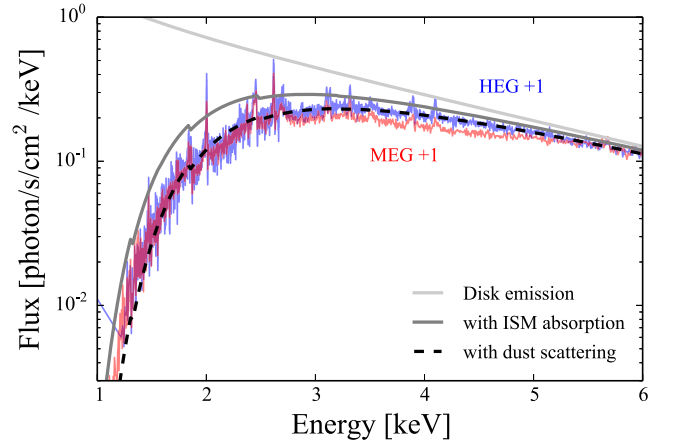


**Figure 2.** The 1–6 keV continuum fit to the high-resolution spectrum of Cygnus X-3 uses a `diskpn` model for the accretion disc emission, `TBnew` for the effect of ISM absorption, and a dust extinction model utilizing RG–Drude scattering.

here forward, we choose to model Cyg X-3 using the HEG arms only, which we presume is accurate on the 5 per cent level.

The magnitude of ISM extinction prohibits precise modelling of the unabsorbed spectrum of Cyg X-3 over the *Chandra* energy range. We found that a pseudo-Newtonian accretion disc emission model appropriate for many HMXBs, `diskpn` (Gierliński et al. 1999), fit the spectrum slightly better than a single power law. However, we did not attempt to model other effects such as Compton reflection or hybrid plasmas, which would describe the  $E > 6$  keV component of the spectrum (e.g. Szostek, Zdziarski & McCollough 2008; Zdziarski, Misra & Gierliński 2010). The continuum extinction model consists of two components: neutral ISM absorption (`TBnew`; Wilms, Allen & McCray 2000; Juett, Schulz & Chakrabarty 2004; Juett et al. 2006) and dust scattering, which will remove light from the spectrum extraction region. As a first-order approximation, we use a custom dust scattering model that follows  $\exp(-\tau_{\text{sca}})$ , where  $\tau_{\text{sca}}$  was calculated by choosing a dust-to-gas mass ratio typical of the Milky Way (0.009; e.g. Draine 2011) and tying it to the ISM column in the following way:

$$\tau_{\text{sca}} \approx 0.009 N_{\text{H}} m_{\text{p}} \kappa_{\text{keV}} E_{\text{keV}}^{-2}. \quad (7)$$

Here,  $\kappa_{\text{keV}} \approx 3.3 \times 10^3 \text{ g}^{-1} \text{ cm}^2$  is the 1 keV scattering opacity from an MRN distribution of dust with  $a_{\text{max}} = 0.25 \mu\text{m}$ , and  $N_{\text{H}}$  is the ISM column from `TBnew`.

Fig. 2 shows the relative contributions of the source model, ISM absorption, and dust scattering for a fit to the 1–6 keV energy range. The best-fitting ISM column is  $N_{\text{H}} \approx 4.3 \times 10^{22} \text{ cm}^{-2}$ , implying  $\tau_{\text{sca}}(1 \text{ keV}) \approx 2$ . This is roughly consistent with the results of the Predehl & Schmitt (1995) study.

We also noted through the course of examination that the fit to the broad 1–6 keV energy band shown in Fig. 2 is systematically low by about 10 per cent around 2 keV and 40 per cent at the softest energy, around 1.25 keV. This is due to the time variation in Cyg X-3, which experiences absorption from its stellar companion (Section 4.4), so the time integrated spectrum may be better represented by a partial covering model. For the purposes of creating a PSF template and extracting a scattering halo, we simply need an accurate measurement of the photon flux. We fit a power law to each 0.5 keV wide energy band between 1 and 3 keV to get the flux for these respective bins.

## 2.2 PSF templates

The High-Resolution Mirror Assembly (HRMA) on *Chandra* focuses about 90 per cent of the X-ray light into a few pixel (2 arcsec) region. The PSF is composed of two parts: the core, where the majority of light is focused, and the wings, where light is spread diffusely due to scattering off of fine surface features in the mirror. Correctly subtracting the PSF from the image is of utmost importance for determining scattering halo profile, the brightness of which is often of the order of the PSF wing brightness. The PSF can be simulated with *Chandra* calibration tools (ChaRT and MARX), but these methods are known to underpredict the wing brightness by a factor of 2–10 (Smith, Edgar & Shafer 2002).

A PSF template may be created from a bright source with a relatively dust-free sight line, but the situation is complicated by the non-linear response of the CCD detectors on *Chandra*. When more than one X-ray photon hits a pixel before the CCD is read out, the resulting electron cloud will be interpreted as either a single photon of larger energy or as a cosmic ray. This effect is known as pileup, and it occurs for any source with a flux of the order of one photon per readout time (typically 3.2 s). For grating-free observations, pileup prevents the correct normalization of a PSF template. However, pileup is mitigated for sources imaged with the HETG in place, both because the effective area is reduced and because a more accurate pile-up free spectrum can be extracted from the grating-dispersed light.

We chose an HETG observation of 3C 273 (ObsId 459) to create a template of the PSF wings. 3C 273 is a bright quasar situated above the Galactic plane; consequently it has a low ISM column ( $N_H \approx 10^{20} \text{ cm}^{-2}$ , inferred from Schlegel, Finkbeiner & Davis 1998). We built a PSF template by extracting a surface brightness profile of the zeroth-order image using  $\Delta E = 0.5 \text{ keV}$  bins between 1 and 6 keV.<sup>2</sup> The average background level for each image was estimated from a region of the S3 chip, about 5.5 arcmin from 3C 273, then subtracted. Using a power-law fit to the HETG spectrum, we also made 0.1 keV binned weighted exposure maps for each image. To create a template, each background subtracted surface brightness profile ( $\mathcal{SB}$ ) was normalized by the effective area from the exposure maps, determined from a small region enclosing the point source ( $\mathcal{A}_{ps}$ ), and by the flux of 3C 273 as measured by the HETG fit ( $F_{ps}$ ):

$$\Psi_{psf}(r, \Delta E) = \frac{\mathcal{SB}(r, \Delta E)}{F_{ps}(\Delta E) \mathcal{A}_{ps}(\Delta E)}. \quad (8)$$

The PSF for Cyg X-3 was then constructed by scaling each template by the point source flux and effective area of Cyg X-3:

$$\mathcal{SB}_{psf}(r) = \sum_E \Psi_{psf}(r, \Delta E) F_{ps}^{X3}(\Delta E) \mathcal{A}_{ps}^{X3}(\Delta E). \quad (9)$$

As an aside, we chose to use PSF templates as opposed to the PSF models by Gaetz et al. (2004) and Gaetz (2010). This is because, upon comparing the CCD extracted spectrum from the zeroth-order image of Her X-1 (ObsId 2749) to the HETG dispersed spectrum, we found that approximately 40 per cent of the zeroth-order photons suffered from pileup effects. This is much larger than the original <5 per cent pileup fraction surmised by Gaetz et al. (2004) based on grade migration and the number of counts per frame. Similarly, we do not use the CXC calibration memo by Gaetz (2010)<sup>3</sup> because

<sup>2</sup> 3C 273 has a small jet feature, which was masked out of the surface brightness profile.

<sup>3</sup> [http://cxc.harvard.edu/cal/Acis/Papers/wing\\_analysis\\_rev1b.pdf](http://cxc.harvard.edu/cal/Acis/Papers/wing_analysis_rev1b.pdf)

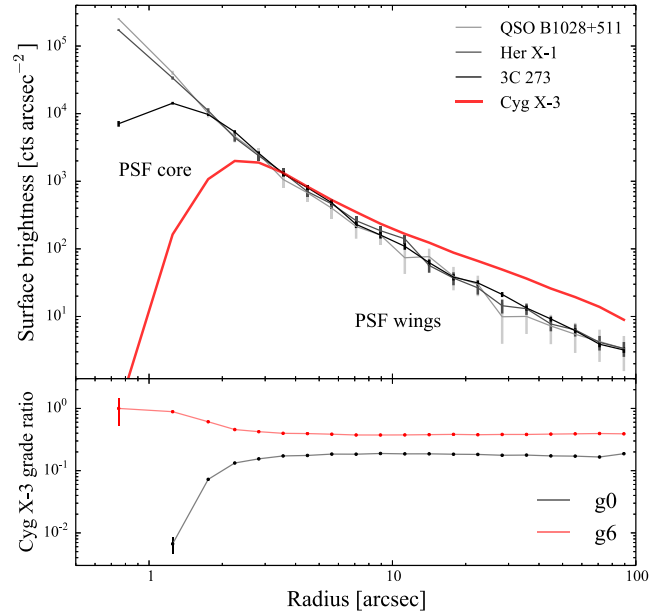


**Figure 3.** Top: a comparison of PSF templates for Cyg X-3 (1–6 keV) using various dust-free sight lines. Bottom: grade migration can be gauged by measuring the ratio of ideal (grade 0) and least acceptable (grade 6) events relative to the total number of all acceptable grades (0, 2, 3, 4, and 6). The abrupt decrease in ideal events (black) and increase in least acceptable events (red) shows that pileup is mainly limited to the inner 3 arcsec of the Cyg X-3 surface brightness profile.

we consider the spectrum determined from HETG dispersed light more reliable than that determined from the ACIS transfer streak for the purposes of normalizing the *Chandra* PSF. Additionally, Gaetz (2010) addresses variations in the PSF wings at larger angular distances (out to 500 arcsec) than those concerned in this work. Our results are more sensitive to the shape of the PSF around the core-wing transition.

To demonstrate the reliability of the template method presented here, we performed the same template construction with two other dust-free sources: Her X-1 (ObsId 2749) and QSO B1028+511 (ObsId 3472). As shown in Fig. 3, each image suffers from varying degrees of pileup, but the PSF wings are relatively stable. The largest deviations occur with QSO B1028+511, which is the dimmest of all three and lacks signal at higher energies. Since 3C 273 is the brightest and has the most signal, we used it to extract the residual surface brightness profile.

## 2.3 Scattering halo extraction

Fig. 3 shows the surface brightness profile of Cyg X-3 relative to the PSF template. Due to its extreme brightness, the centre of Cyg X-3 is hollowed out, and much of the information is lost due to the non-linear effect of detector pileup. We test to what extent pileup affects the wings of the Cyg X-3 profile by examining the event grades – numbers assigned according to the shape of the electron cloud produced by a high-energy event. When multiple X-ray photons hit one region of the detector, the resultant electron cloud is likely to be asymmetric, leading to grade migration – the assignment of a larger numeric value to what would otherwise be a normal (grade 0) event. The bottom portion of Fig. 3 shows that grade migration is most noticeable within 3 arcsec, which is about the point at which the surface brightness of Cyg X-3 dips below the PSF template. McCollough, Smith & Valencic (2013, fig. 1) also



find that the surface brightness profile of Cyg X-3 suffers pileup fractions less than 5 per cent for  $r > 3$  arcsec and less than 1 per cent for  $r > 8$  arcsec. Pileup is therefore has a negligible effect on the dust scattering halo, which we extract for observation angles larger than 5 arcsec.

The typical 0.5–7 keV background<sup>4</sup> for a 50 ks observation on the S3<sup>5</sup> CCD chip is 0.02 counts  $\text{pix}^{-1}$ , or 0.03 counts  $\text{pix}^{-1}$  for the 5–10 keV background. This is two orders of magnitude below the dimmest portion of the Cyg X-3 surface brightness profile, suggesting that all the ambient light comes from X-ray scattering. Since the quiescent detector background is minuscule by comparison, it was not included in this analysis.

There is a Bok globule located 16 arcsec from Cyg X-3, observed from X-ray scattering (McCollough et al. 2013). A 3 by 4.5 arcsec region covering the globule contains 7120 counts, which accounts for approximately 30 per cent of the total brightness at that radius. We removed the globule from the measurement, because the halo model assumes azimuthal symmetry. We also excised from the zeroth-order image a 2.5 arcsec wide region containing the CCD transfer streak.

The scattering halo measured from the zeroth-order image might also be contaminated from the first-order halo dispersed by the HETG. To test this, we extracted a radial surface brightness profile from a rectangular region oriented in the MEG dispersion direction. There was evidence of contamination from the MEG first-order scattering halo in regions  $>50$  arcsec away from the point source centre, differing by  $4\sigma$  at the outermost annulus. We therefore chose to confine the surface brightness profiles to a rectangular region perpendicular to both the MEG and HEG arms.<sup>6</sup> This choice did not lead to any significant loss in signal, since the outer edges of the halo are covered by annuli of larger surface area.

When examining the extended image of Cyg X-3, one cannot discern whether a given photon was scattered by dust or by the *Chandra* mirrors; each type is subject to a different effective area. Aside from uneven quantum efficiencies in the CCD chip, a mirror-scattered X-ray event should be corrected by the effective area for the point source image. A dust-scattered X-ray event should be corrected by the effective area of the detector at the position of the event. Normalizing the entire image by an exposure map created with standard calibration techniques would thereby produce an inaccurate image of both the PSF and the scattering halo. This is why we chose to scale the PSF templates by point source effective area ( $\mathcal{A}_{\text{ps}}$ ) to obtain a raw counts surface brightness profile such as that seen in Fig. 3. Since all of the HETG objects used in this study used standard HETG pointings, within 30 arcsec of the detector focal point, we expect the overall effect of quantum inefficiencies (dead pixels and columns) to be relatively similar.

We extracted residual surface brightness profiles, containing the raw counts from dust scattering alone, for each 0.5 keV binned image. Then we extracted radial profiles from exposure maps using the same window described above. The exposure maps used in this case were calculated for a single energy, not weighted, because the spectral energy distribution for the scattered light is much different from the point source. We also could not apply weights in this

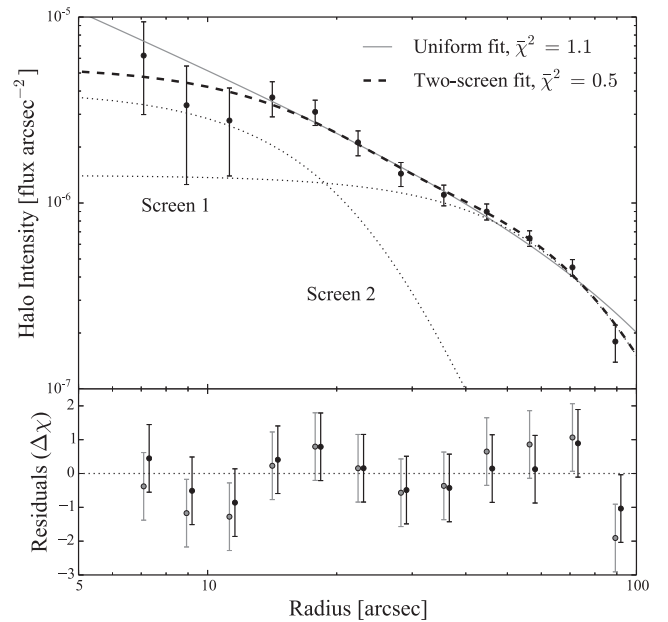


**Figure 4.** The 4–6 keV scattering halo intensity. Top: overlaid are the best EMCEE model fits for dust distributed uniformly along the line of sight (grey solid line) and for dust contained in two screens (black dashed line), corresponding roughly to the positions of foreground spiral arms of the Milky Way. Bottom: the residuals for the best uniform (light points) and two-screen fits (dark points) are plotted in units of sigma. The two-screen residuals are offset horizontally to aid visibility.

case because the energy distribution should change depending on the angular distance from the point source (cf. equation 3). After normalizing each annulus by the mean effective area, the residual profiles were summed via

$$I_h(r) = \sum_{\Delta E} \frac{\mathcal{SB}(r, \Delta E) - \mathcal{SB}_{\text{psf}}(r, \Delta E)}{\mathcal{A}(r, \Delta E)} \quad (10)$$

to produce the 4–6 keV halo intensity profile plotted in Fig. 4. The zeroth-order image of Cyg X-3 is much more piled up than 3C 273, which does not have a hollowed out core. We threw out data points from bins where the PSF template exceeded the observed surface brightness and kept data points with a signal to noise  $> 1$ .

### 3 FIT TO 4–6 KEV HALO PROFILE

Our fit to the scattering halo profile, shown in Fig. 4, rests upon three fundamental assumptions.

(i) *Single scattering.* The large optical depth to scattering implies that a significant fraction of photons will scatter more than once. We take a conservative route by restricting analysis to an energy band where the scattering halo intensity is well within the optically thin, single scattering regime:  $E > 4$  keV, i.e.  $\tau_{\text{sca}} \lesssim 10$  per cent.

(ii) *RG–Drude scattering from grains of a single density.* In this scattering regime, the dust grain composition is not very important because each grain is approximated as a sphere of free electrons. We assume a grain density  $\rho = 3 \text{ g cm}^{-3}$ , which is the average between graphite and silicate materials (Draine 2011). The RG–Drude scattering cross-section is featureless and follows a power-law dependence on energy. However, the true dielectric functions will cause absorption and scattering resonances that diverge significantly from the RG–Drude approximation at low energies (Section 4). Restricting the energy range to 4–6 keV also alleviates the need to use the

<sup>4</sup> *Chandra* Proposer’s Observing Guide, Table 6.10, <http://cxc.harvard.edu/proposer/POG/>

<sup>5</sup> The ACIS S3 chip contains the zeroth-order image for the nominal HETG pointing.

<sup>6</sup> Surface brightness measurements with annuli  $\alpha < 20$  arcsec receive full azimuthal coverage.

more accurate, and more computationally intensive, Mie scattering cross-section.

(iii) *A power-law grain size distribution.* Since a power law provides a computationally efficient means to calculate the scattering halo intensity (equation 4, see appendix), we adopt the simplifying assumption that a power law is a good first-order approximation to the dust grain size distribution. For dust distributed uniformly along the line of sight ( $\xi = 1$ ),

$$I_h(\alpha, E) = \frac{F_a}{\sqrt{8\pi}} \frac{\tau_{\text{sca}}}{\alpha \tilde{\sigma}_0(E)} \frac{G_u(a, p, \alpha, E)}{G_p(a, p)}, \quad (11)$$

where  $\tilde{\sigma}_0 = 1.04 \text{ arcsec } E_{\text{keV}}^{-1}$ ,  $G_p$  is an integral over a power law, and  $G_u$  is a function of erf and incomplete gamma functions as defined in the appendix. For an infinitesimally thin dust screen, where  $\xi = \delta(x - x_s)$ ,

$$I_h(\alpha, E) = \frac{F_a}{x_s^2} \frac{\tau_{\text{sca}}}{2\pi \tilde{\sigma}_0^2(E)} \frac{G_s(a, p, \alpha, x_s, E)}{G_p(a, p)} \quad (12)$$

which is also described in the appendix. Screens produce a flat surface brightness profile, and a uniform distribution produces a cuspy profile.

As mentioned in Section 2.1, the high-resolution imaging capabilities of *Chandra* imply that the spectrum extracted from the HETG dispersed light is also reduced by extinction from dust scattering. To correct for this, we modify the point source flux  $F_{\text{ps}}$  by the model  $\tau_{\text{sca}}$  value to calculate the scattering halo intensity, which is proportional to  $F_a = F_{\text{ps}} e^{\tau_{\text{sca}}}$ .

We use the publicly available Markov Chain Monte Carlo (MCMC) code *EMCEE* to explore the parameter space in a Bayesian analysis of possible halo fits (Foreman-Mackey et al. 2013). To see what X-ray scattering can tell us about the large end of the grain size distribution, we freeze the low end of the distribution at  $0.005 \mu\text{m}$  and fit for  $a_{\text{max}}$  and  $p$ . At a fixed energy, the dust grain distribution parameters  $a_{\text{max}}$  and  $p$  mainly affect the scattering halo shape. The optical depth to scattering mainly controls the halo normalization, which scales with the total dust mass column,  $\tau_{\text{sca}} = \kappa_{\text{sca}}(a, p) M_d$ . We use  $N_H$  as a free parameter and convert to  $M_d$  using the dust-to-gas mass ratio of 0.009.

### 3.1 Uniform fit

We start with uniformly distributed dust because it has the least number of free parameters and will likely match the shape of the halo profile, which appears cuspy. We assigned uniform priors to  $\log(N_H)$  from 14 to 24  $\text{cm}^{-2}$  and  $a_{\text{max}}$  from  $0.01$ – $0.5 \mu\text{m}$ . We found that, if  $p$  was allowed to take on large values, the halo fit solution became highly degenerate for  $a_{\text{max}} > 0.3 \mu\text{m}$ . A large grain size cut-off value required increasingly steep power laws,  $p > 5$ , so that the small end of the size distribution greatly dominates. To suppress these uninformative degenerate solutions, we assigned a Gaussian prior to  $p$  with mean 3.5 and standard deviation 0.5.

We used 100 walkers in *EMCEE* to obtain  $10^4$  independent samples of the posterior distribution, shown in Fig. 5. Two-dimensional histograms comparing each parameter against the others illustrates that they are highly covariant. The total scattering optical depth was calculated for each sample point in the posterior distribution. The vertical dashed lines indicate the 16th, 50th, and 84th quantiles – corresponding to the median and  $1\sigma$  confidence interval. Fig. 4 plots the best model halo corresponding to the smallest  $\bar{\chi}^2$  obtained from the posterior distribution. The best fit, median fit, and  $1\sigma$  confidence intervals are listed in Table 1.

### 3.2 Scattering from dust screens

X-ray scattering can probe galactic structure in the direction of Cyg X-3, which might include features such as those associated with Cyg OB2 or Galactic spiral arms (Section 1.2). When applying the infinitesimally thin screen model, it should be kept in mind that while the total integrated halo flux will be fixed according to the optical depth of the screen, the surface brightness profile will vary according to the screen's position. For screens closer to the observer (large  $x$ , see Fig. 1), the scattered flux will be spread over a large area, reducing the overall surface brightness profile. When a screen is close to the X-ray source (small  $x$ ), the halo surface brightness profile will be more compact and thus brighter close to the point source.

Taking 9 kpc as the best estimate for the distance to Cyg X-3, we expect the Perseus arm, about 5–6 kpc away (Reid et al. 2014), to correspond to a screen with  $x_s \approx 0.4$ . The outer spiral arm, if in the foreground of Cyg X-3, will be at  $x_s \leq 0.1$  and would therefore contribute most to the surface brightness profile. The Cyg OB2 association, 1.4 kpc away (Rygl et al. 2012), corresponds to  $x_s \approx 0.8$  and would contribute to the outermost portion of the profile.

We attempt to fit a model halo with the least number of dust screens, in this case two. In the optically thin regime, the intensity of the halo from each screen can simply be added to get the total observed halo. We ran *EMCEE* with a six parameter model containing two screen positions ( $x_1$  and  $x_2$ ) and their respective ISM columns ( $N_{H,1}$  and  $N_{H,2}$ ), assuming the same dust grain distribution for both screens ( $a_{\text{max}}$  and  $p$ ).

We evaluated potential screen positions, finding that an MRN distribution of dust associated with the Cyg OB2 region would create a halo intensity  $\sim 1 \text{ count pix}^{-1}$ , which is too dim to contribute significantly. We omit it from analysis. We chose a Gaussian prior with mean 0.4 and standard deviation 0.1 applied to  $x_1$  is used to model the Perseus arm. To get at the inner portion of the scattering halo, which we believe is associated with the Milky Way outer spiral arm, we applied a Gaussian prior to  $x_2$  with mean 0.05 and standard deviation 0.1. The spread in these distributions accounts roughly for the uncertainty in the distance to Cyg X-3,  $9_{-2}^{+4}$  kpc (Predehl et al. 2000). The prior distributions on  $x_1$  and  $x_2$  were truncated at 0.23, so that  $x_1$  always represents the screen closer to the observer. The priors on  $N_H$ ,  $a_{\text{max}}$ , and  $p$  are identical to those in Section 3.1.

Fig. 4 shows the best fit according to smallest  $\bar{\chi}^2$  drawn from the posterior distribution. The relative contribution of each screen is also plotted. Two-dimensional histograms displaying the covariances among each parameter are presented in Fig. 6. Table 2 lists the best, median, and  $1\sigma$  confidence intervals for each parameter in the two screen fit, including the total dust mass and scattering optical depth.

## 4 ENERGY RESOLVED SCATTERING HALOES

The ratio between the scattering halo flux  $F_h = F_a(1 - e^{-\tau_{\text{sca}}})$  and the point source  $F_{\text{ps}} = F_a e^{-\tau_{\text{sca}}}$  serves as a direct measurement for the energy dependence of the scattering cross-section via

$$\frac{F_h}{F_{\text{ps}}} = e^{\tau_{\text{sca}}} - 1. \quad (13)$$

We aim to measure this quantity from the energy resolved scattering haloes extracted from ObsId 6601 in the range of 1–6 keV, to test how well the 4–6 keV fits from Section 3 do to approach a fully consistent halo model across a wide range of energies.

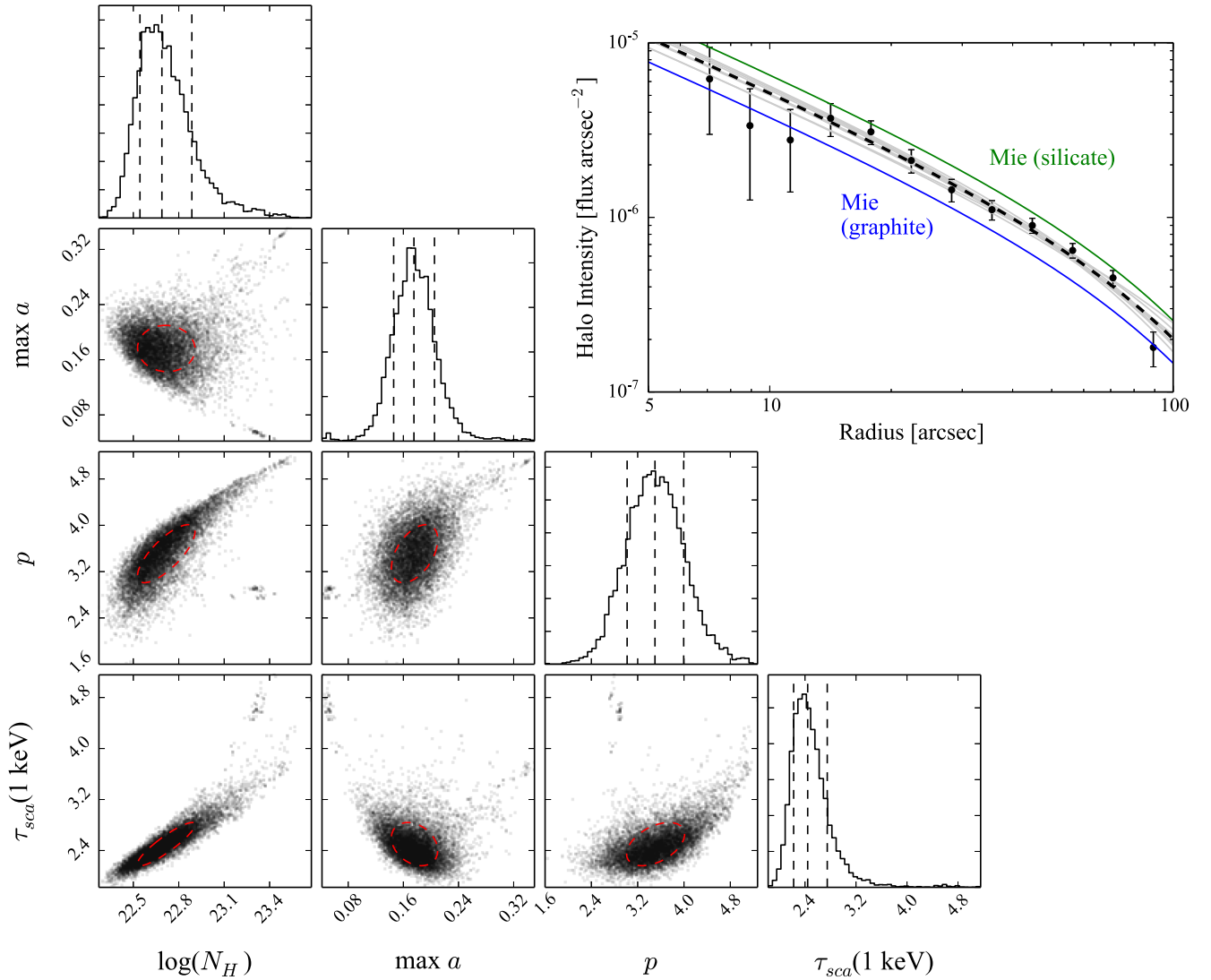


**Figure 5.** The posterior distribution from EMCEE is plotted with two-dimensional histograms comparing each pair of free parameters ( $N_H$ ,  $p$ , and  $a_{\max}$ ) and the resulting  $\tau_{\text{sca}}$  distribution. There is particularly strong covariance between power-law exponent  $p$  and ISM column  $N_H$ , making  $\tau_{\text{sca}}$  covariant with both these parameters. The vertical dashed lines in each one-dimensional histogram mark the median and  $1\sigma$  confidence interval for each parameter; the red dashed ellipses indicate the  $1\sigma$  confidence intervals in two-dimensional space. The upper-right hand figure shows the best-fitting EMCEE walker (black dashed line) in comparison to 10 other walkers in the posterior distribution (solid grey lines). Using the best-fitting walker from Table 1, the scattering halo intensities calculated with the Mie scattering cross-section for all graphite (blue) or all silicate (green) dust grains straddle the RG-Drude solution.

**Table 1.** Uniform fit to dust scattering halo (4–6 keV).

	Best	Median	( $1\sigma$ C.I.)	Units
$N_H$ :	3.0	4.9	(3.5, 7.7)	$10^{22} \text{ cm}^{-2}$
$a_{\max}$ :	0.15	0.18	(0.15, 0.21)	$\mu\text{m}$
$p$ :	2.1	3.5	(3.0, 4.0)	
$\tau_{\text{sca}} E^2$ :	2.2	2.4	(2.2, 2.7)	$\text{keV}^2$

However, the field of view in ObsId 6601 is limited to about 4 arcmin along the axis perpendicular to the grating dispersion direction. Our measured  $F_h/F_{\text{ps}}$  value will be lower because only a fraction of the total scattering halo is being captured. Defining  $\alpha_1 = 6.25$  arcsec and  $\alpha_2 = 99.5$  arcsec from the angular limits of

the extracted scattering halo profiles (Fig. 4), the fraction of halo light captured is

$$f_{\text{cap}}(E) \equiv \frac{\int_{\alpha_1}^{\alpha_2} I_h(\alpha, E) 2\pi\alpha d\alpha}{F_a(1 - e^{-\tau_{\text{sca}}})}. \quad (14)$$

Multiplying equations (13) and (14) together, the observed flux ratio will be

$$\frac{F_h^{\text{cap}}}{F_{\text{ps}}} = e^{\tau_{\text{sca}}} \int_{\alpha_1}^{\alpha_2} \frac{d\psi_h}{d\Omega}(\alpha, E) 2\pi\alpha d\alpha. \quad (15)$$

So in order to compute  $F_h^{\text{cap}}/F_{\text{ps}}$ , one must compute a scattering halo model to account for missing flux. A field of view of the order of 10–20 arcmin is necessary to capture the vast majority of halo light, thereby obtaining a model independent measurement for  $\tau_{\text{sca}}$ .

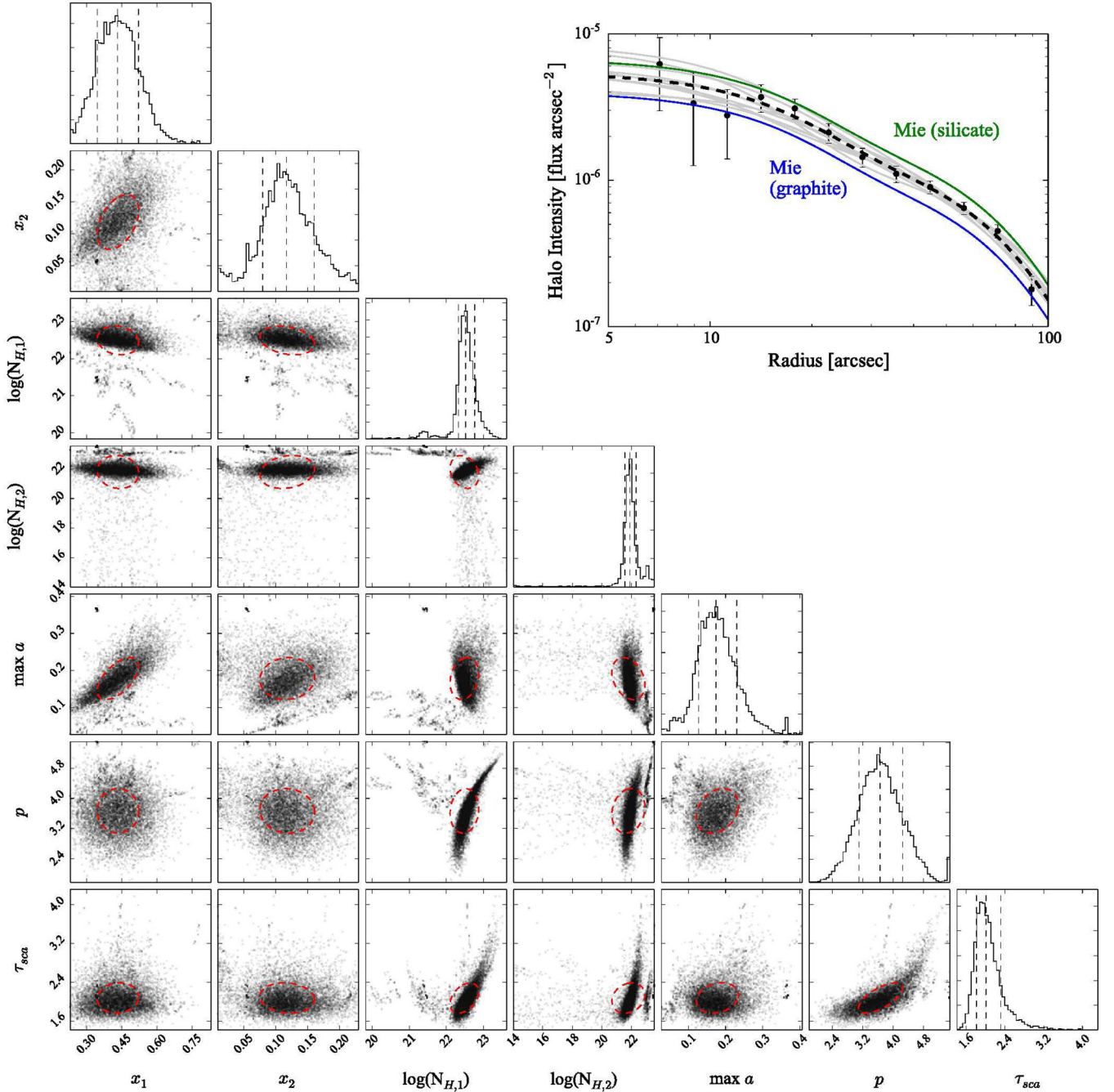


**Figure 6.** The posterior distribution from EMCEE is plotted with two-dimensional histograms comparing each pair of free parameters (screen positions, respective  $N_{\text{H}}$ ,  $p$ , and  $a_{\text{max}}$ ) and the resulting  $\tau_{\text{sca}}$  distribution. The vertical dashed lines in each one-dimensional histogram mark the median and  $1\sigma$  confidence interval for each parameter; the red dashed ellipses indicate the  $1\sigma$  confidence intervals in two-dimensional space. The upper-right hand figure shows the best-fitting EMCEE walker (black dashed line) in comparison to 10 other walkers in the posterior distribution (solid grey lines). Using the best-fitting walker from Table 2, the scattering halo intensities calculated with the Mie scattering cross-section for all graphite (blue) or all silicate (green) dust grains straddle the RG–Drude solution.

We split ObsId 6601 into energy separated images using 0.5 keV wide bins going from 1 to 6 keV.  $F_{\text{h}}^{\text{cap}}$  was calculated by summing the flux in each annulus, after applying the same PSF and background subtraction methods described in Section 2,

$$F_{\text{h}}^{\text{cap}}(\Delta E) = \sum_{\alpha_1 \leq r \leq \alpha_2} \frac{SB(r, \Delta E) - SB_{\text{psf}}(r, \Delta E)}{\mathcal{A}(r, \Delta E)} \quad (16)$$

but only including annuli where the residual surface brightness was positive. The  $F_{\text{ps}}$  value was obtained by integrating the HETG fit described in Section 2.1.

The grey and black dashed curves in Fig. 7 show the observed flux ratios in comparison to that predicted from the 4–6 keV models fit in Section 3. For energy bins below 2.5 keV, the observed scattering halo flux is about a factor of 2–3 lower than that predicted from the scattering models used thus far. We explore possible explanations



**Table 2.** Two screen fit to dust scattering halo (4–6 keV).

	Best	Median	(1 $\sigma$ C.I.)	Units
Screen 1				
$x_1$	0.59	0.43	(0.35, 0.53)	
$N_{H,1}$	1.5	3.3	(2.1, 5.8)	$10^{22} \text{ cm}^{-2}$
Screen 2				
$x_2$	0.16	0.12	(0.08, 0.16)	
$N_{H,2}$	0.3	0.8	(0.4, 2.0)	$10^{22} \text{ cm}^{-2}$
Dust distribution				
$a_{\text{max}}$	0.21	0.17	(0.13, 0.23)	$\mu\text{m}$
$p$	2.4	3.6	(3.1, 4.2)	
Total $N_H$	1.8	4.1	(2.8, 6.9)	$10^{22} \text{ cm}^{-2}$
$\tau_{\text{sca}} E^2$	1.8	2.0	(1.8, 2.3)	$\text{keV}^2$

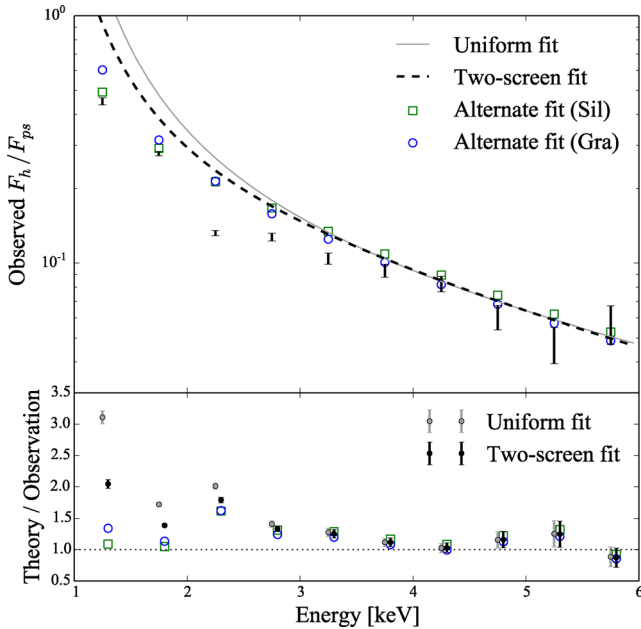


**Figure 7.** The ratio of halo flux ( $F_h$ , observed within  $\approx 6$ –100 arcsec) to point source flux ( $F_{\text{ps}}$ ) of Cyg X-3. The solid grey and dashed black lines show theoretical expectations for the lowest  $\chi^2$  fit for uniform and two-screen dust distributions, respectively. The bottom portion of the figure plots the ratio of theory to observation, showing that theoretical cross-section overpredicts the amount of soft-energy scattering by a factor of 2–3. The open circles and squares show the predicted ratios from Mie scattering calculations of graphite and silicate grains using an alternate fit to the 4–6 keV halo that incorporates large dust grains  $\sim 1.5 \mu\text{m}$  in the vicinity of the Cyg OB2 association (Section 5.2).

for this behaviour below, including an alternative fit to the 4–6 keV scattering halo that utilizes large dust grains. This alternative is plotted with open circles and squares in Fig. 7 and will be explained below in Section 5.2.

#### 4.1 Multiple scattering

As shown in Sections 2.1 and 3, the sight line to Cyg X-3 is optically thick to dust scattering for much of the energy range of interest. However, the calculations performed thus far only include the halo image from photons that scatter once through the intervening ISM. Higher order scattering terms would alter the halo surface brightness

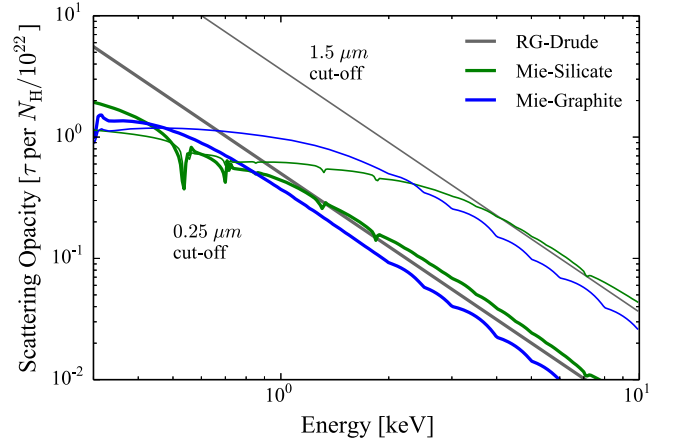


**Figure 8.** Comparison between the RG-Drude (grey) and Mie scattering (blue and green) optical depth per  $N_H = 10^{22} \text{ cm}^{-2}$  for an MRN distribution of dust grains with  $a_{\text{max}} = 0.25 \mu\text{m}$ , typical for Milky Way diffuse ISM (thick lines). When  $a_{\text{max}} \gtrsim E_{\text{keV}}$ , the RG-Drude approximation is no longer valid, and the Mie scattering solution shows that the scattering cross-section is significantly reduced at softer energies. An experimental dust grain size distribution with the same power-law slope but  $a_{\text{max}} = 1.5 \mu\text{m}$  shows how increasing the grain size can cause the dust scattering optical depth to be reduced significantly for  $E < 3 \text{ keV}$  (thin lines).

profile in two ways: (i) increasing the intensity (equation 13), and (ii) creating a more extended scattering image. For more details, we refer the reader to Mathis & Lee (1991).

How do higher order scattering effects alter the predicted  $F_h^{\text{cap}}/F_{\text{ps}}$  curves? Taylor expanding equation (13) gives an estimate for the relative flux contribution from each higher order halo:  $F_{h1} \propto \tau_{\text{sca}}$ ,  $F_{h2} \propto \tau_{\text{sca}}^2/2$ , and so on. Inclusion of higher order scattering terms would thereby increase model  $F_h/F_{\text{ps}}$  by a factor  $\sim \tau_{\text{sca}}/2$ , which does not resolve the behaviour of the data points in Fig. 7.

In addition, Smith et al. (2006) show that the second-order scattering haloes for MRN dust and  $N_H = 4 \times 10^{22} \text{ cm}^{-2}$  increases the intensity of the inner halo ( $\alpha < 100 \text{ arcsec}$ ) only by about 5 per cent and has little effect on the profile shape in that region. This means that our  $F_h^{\text{cap}}$  value is likely accurate to within 5–10 per cent. Note also that, in equation (14), the denominator holds true for the optically thick case; higher order scattering terms will only affect the numerator in the equation. From these observations, we conclude that our predicted  $F_h^{\text{cap}}/F_{\text{ps}}$  curves would not change significantly with the inclusion of higher order scattering effects.

#### 4.2 Scattering contribution from large grains

The downturn in observed  $F_h^{\text{cap}}/F_h$  data points at low energies may be indicative of a population of large dust grains. This is because the RG-Drude approximation breaks down when the grains become too large in comparison to the photon energy, violating the general rule-of-thumb  $a_{\text{um}} \lesssim E_{\text{keV}}$  (Smith & Dwek 1998). Fig. 8 shows how the Mie scattering solution (Bohren & Huffman 1983) for two commonly hypothesized grain materials, silicate and graphite (Draine 2003b), departs from the RG-Drude approximation at low photon energies. Using a power-law slope of  $-3.5$ , the Mie scattering solutions produce much lower cross-sections for  $E \lesssim 1 \text{ keV}$  when the grain size cut-off is  $a_{\text{max}} = 0.25 \mu\text{m}$ , or for  $E \lesssim 3 \text{ keV}$  when  $a_{\text{max}} = 1.5 \mu\text{m}$ .

There is reason to believe that grains larger than a few tenths of a micron exist along the Cyg X-3 sight line. The cold and dense environments of molecular clouds, such as the foreground Cygnus X molecular region, are likely to be a location of grain growth (Draine 2003a). Evidence for micron-scale grains in molecular cloud cores has been observed through the infrared scattering phenomenon, or ‘coreshine’ (e.g. Steinacker et al. 2010; Andersen et al. 2013). While not likely associated with Cygnus X, the existence of a Bok globule imaged with X-ray scattering (McCollough et al. 2013) also offers circumstantial evidence that large grains may obscure the sight line of Cyg X-3. In addition, the foreground young stellar association Cyg OB2 contains a number of Wolf–Rayet and candidate evolved stars (Comerón et al. 2002). These types of stars experience significant mass-loss in the form of dusty winds, causing large amounts of extinction,  $A_V = 3\text{--}10$  (Wright et al. 2015). The stellar winds of evolved stars are also likely sites for grain growth, and there is some evidence for micron-sized grains in evolved circumstellar environments (de Vries et al. 2015).

Unfortunately, calculating the halo intensity with Mie scattering is computationally intensive, preventing a Bayesian analysis of the full range of energy resolved scattering haloes at this time. A comparison of the Mie scattering halo intensity using the best-fitting parameters of Sections 3.1 and 3.2 are shown in Figs 5 and 6. As expected from Fig. 8, the Mie scattering haloes from dust distributions of pure silicate or pure graphite grains straddle the RG–Drude approximation. In Section 5.2, we use RG–Drude to explore a fit to the 4–6 keV halo that includes micron-sized grains, then extrapolate that fit to the lower energy band with Mie scattering.

### 4.3 Dust optical properties

Another possibility is that some population of dust grains in the foreground of Cyg X-3 have different optical properties than those used in this work (graphite and astrosilicate from Draine 2003b). This could include composite grain types ZDA, core-mantle grains (Li & Greenberg 1997), or elongated grains (e.g. Min, Hovenier & de Koter 2003). Porous, ‘fluffy’ grains will reduce the scattering cross-section because they have a lower material density ( $\rho_3$  in equation 1). However, the cross-section should still roughly follow the  $E^{-2}$  power law for instances where the RG–Drude approximation holds. Fluffy grains are thereby expected to change the normalization but not the qualitative behaviour of the curves in Fig. 8.

Regardless, the data in Fig. 7 show that the soft X-ray extinction properties of interstellar dust differ significantly from the often used RG–Drude approximation. A future study incorporating a wider field of view, encompassing the entire scattering halo of Cyg X-3, would provide a direct measurement of the energy dependence of the dust scattering cross-section.

### 4.4 Time variation and pileup in Cyg X-3

Cyg X-3 is a binary exhibiting deep absorption minima on a 4.8 h period (Brinkman et al. 1972), making it a good object for studying scattering in the time domain. Since the scattered light takes a longer path, there is a delay between non-scattered and scattered light. Predehl et al. (2000) used the first *Chandra* observations of Cyg X-3 to determine a geometric distance of  $9^{+4}_{-2}$  kpc. ObsId 6601 is 49.6 ks long and covers 2.9 cycles of the Cyg X-3 period, as opposed to the 12.3 ks observation used by Predehl et al. (2000), which covers only 0.7 cycles. Given that ObsId 6601 contains nearly an integer number of cycles, we used the time-integrated image under the assumption

that the average brightness of the point source describes the average brightness of the scattering halo.

To check that this assumption is valid, we divided ObsId 6601 into time intervals when Cyg X-3 was brightest ( $1\sigma$  above the mean count rate, for a total of 10.76 ks) and dimmest ( $1\sigma$  below the mean count rate, for a total of 11.35 ks). We checked each time interval for pileup. Based on the count rate in the 4–5 keV region, we expect that roughly 7 per cent of the HEG events are lost due to pileup during the brightest phase, and roughly 2 per cent during the dimmest phase. Such low pileup fractions indicate that the behaviour of the instrument will be nearly linear.

The shape of the Cyg X-3 spectrum also varies with brightness. There is more absorption from the stellar companion in the dim phases of the light curve in comparison to the bright phases. Despite these differences, we found that averaging the spectrum from bright and dim phases yields a curve that is identical to the time-integrated spectrum, to within a few per cent.

Time variations in the scattering halo will only be visible for angles where the time lag is less than the period of the source. In the case of Cyg X-3, this is true for observation angles  $\alpha \leq 40$  arcsec. When we extracted the radial profile from bright and dim time intervals, we indeed found variations in the soft-energy halo out to  $\alpha \sim 20$  arcsec. However, given that (i) the spectral variations of Cyg X-3 scale linearly, and average out to the time integrated spectrum; and (ii) time variations in the scattering halo cannot exceed the period of Cyg X-3; and (iii) the duration of ObsId 6601 covers three whole cycles of the binary period, we conclude that the average time integrated flux computed in Section 2.1 should describe the average time integrated scattering halo in Section 3.

### 4.5 Possible sources of systematic error

Only two of the data points, one at 4.75 keV and the other at 5.25 keV, are systematically low because they contain some negative residual surface brightness values, causing a few annular bins to be ignored from equation (16).

The abrupt decrease in scattering halo flux may be partly due to instrumental effects. The Al-K and Ir-M absorption edges cause swift changes in the telescope effective area around 1.55 and 2.1 keV, respectively. We did our best to correct for this by using weighted exposure maps of the source spectrum to build the PSF templates (Section 2). Si-K and Au-M absorption edges (1.8 and 2 keV) within the CCD and HETG instruments themselves can also remove or alter, through fluorescence, the observed energy of incoming photons in this range. This might contribute to the fact that the 1.75 and 2.25 keV energy bins exhibit the most dramatic discrepancies between model and data.

## 5 EXPLORATION OF ALTERNATIVE FITS

We explored a number of alternative fits to the 4–6 keV scattering halo, in attempts to explain the energy resolved scattering haloes evaluated above. None of them were able to completely fit the scattering halo behaviour in the 1–6 keV range. None the less, we document them here for completeness. Table 3 gives a summary of the best-fitting parameters for alternative two-screen dust scattering halo models.

### 5.1 Two screens with different grain size distributions

We performed a least-squares fit with no priors to the 4–6 keV scattering halo, allowing all parameters to vary so that each dust

**Table 3.** Alternative fits to the 4–6 keV dust scattering halo.

Two screen fit with all parameters free ( $\bar{\chi}^2 = 0.7$ )					
	$x$	$N_H^a$	$a_{\max}^b$	$p$	$\tau_{\text{sca}} E^{2c}$
Screen 1:	0.73	1.0	0.25	1.6	1.4
Screen 2:	0.18	0.6	0.25	3.4	0.4
Two screen fit with large grains in Cyg OB2 ( $\bar{\chi}^2 = 0.6$ )					
	$x$	$N_H^a$	$a_{\max}^b$	$p$	$\tau_{\text{sca}} E^{2c}$
Screen 1:	0.45	3.0	0.18 <sup>d</sup>	3.5 <sup>d</sup>	1.6
Screen 2:	0.78	0.08	1.12	3.0	0.3

<sup>a</sup>10<sup>22</sup> cm<sup>-2</sup>; <sup>b</sup>μm; <sup>c</sup>keV<sup>2</sup>; <sup>d</sup>Fixed model parameter.

screen was allowed to have its own grain size distribution. This requires 60 per cent of the dust to be in a foreground screen with a shallow grain size distribution ( $p = 1.6$ ), so that the majority of the mass is in 0.25 μm grains. The other 40 per cent of the dust follows an MRN distribution and is contained in a screen close to Cyg X-3.

We checked to see if the noticeably shallow grain size distribution for Screen 1 turned away from the RG–Drude approximation at energies larger than 1 keV. The resulting  $\tau_{\text{sca}}$  curve did not differ significantly from the behaviour seen in Fig. 8, showing that the total X-ray scattering cross-section is more sensitive to  $a_{\max}$  than  $p$ . As with the fits presented in Section 3, this model overpredicts the amount of scattering at soft energies.

## 5.2 Large grains in the vicinity of Cyg OB2

Inspired by the Mie scattering cross-sections in Fig. 8, we explored an alternate fit to the 4–6 keV halo that replaces the far screen of dust grains ( $x_2 \approx 0.1$ ) with a hypothesized screen of large grains coextensive with the Cyg OB2 association ( $x_2 \approx 0.8$ ). This nearby scatterer needs to contain grains  $\sim 1$ –2 μm in radius to form the inner portion of the scattering halo, which is mainly confined to a 10 arcsec region. Properties of the dust grain size distribution in the first screen, corresponding to scattering from the Perseus arm, were held fixed using values from Section 3.2. In this model, the screen associated with Cyg OB2 contains only a few per cent of the total dust mass and accounts for about 20 per cent of all scattering for  $E > 4$  keV (where the RG–Drude approximation holds). The posterior distribution median and  $1\sigma$  confidence interval for the grain size cut-off is  $a_{\max} = 1.5^{+0.5}_{-0.4}$  μm.

Fig. 9 shows the scattering halo intensity for the best fit obtained from the posterior distribution (Table 3) in the 1–2.5 keV and 4–6 keV bands. The RG–Drude approximation, used to fit the 4–6 keV halo intensity, is shown for the 1–2.5 keV band as a comparison to the Mie scattering solutions. By including a thin screen of large grains in the foreground, the inner portion of the soft-energy scattering halo drops out by a factor of about 2. There is still a noticeable systematic offset in the outer portion of the scattering halo profile, which is dominated by the more distant (Perseus arm) screen that contains MRN-type dust. The fact that this dust model does not reconcile the energy-resolved scattering haloes entirely emphasizes the need for testing the energy dependence of the dust scattering cross-section over a broader range of X-ray energies.

To incorporate this fit into Fig. 7, we computed the scattering haloes at lower energies using the Mie scattering solution for Screen 2 (Cyg OB2) and the RG–Drude approximation for Screen 1 (Perseus arm). Calculating the Mie scattering haloes is computationally intensive, so we computed them using only the bin centres for each 0.5 keV wide energy band. Fig. 7 illustrates that the inclusion of micron-sized grains brings the predicted halo flux into closer

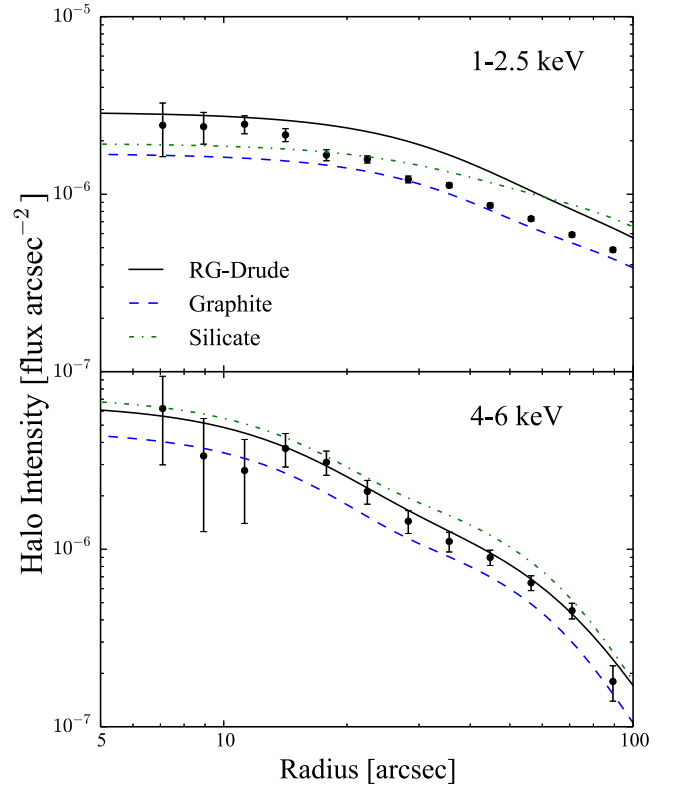


**Figure 9.** X-ray scattering halo intensities from a fit that includes large micron-sized dust grains in the vicinity of the Cyg OB2 association. The 1–2.5 keV curves (top) were extrapolated from the RG–Drude fit to the 4–6 keV scattering halo intensity (bottom). In situations where the RG–Drude approximation is appropriate, the Mie scattering solution for a population of purely silicate (green dash–dotted) or purely graphite (blue dash) grains straddles the RG–Drude solution (black). In the lower energy band where RG–Drude does not hold, the Mie scattering solution produces dimmer scattering haloes overall.

alignment with the observed values. It is also interesting to note that the median  $a_{\max}$  value for this scenario agrees with the models of Wang, Li & Jiang (2014), which show that 1.5 μm sized dust grains can reproduce the mid-IR extinction curve of the Milky Way. However, there is still a huge discrepancy in the 2–2.5 keV bin that remains a mystery. The question of whether this is an instrumental effect or a true ISM absorption feature can be addressed by a study that compares dust scattering haloes from multiple instruments.

## 5.3 Implied extinction

The incorporation of large dust grains for modelling the X-ray scattering halo of Cyg X-3 begs the question: what will the extinction curve look like? ISM extinction curves can vary across different regions of the Milky Way, but they are generally characterized by the magnitude of extinction relative to the colour change:  $R_V \equiv A_V/E(B - V)$  (Cardelli, Clayton & Mathis 1989). Extinction curves with a high  $R_V$  can be produced by extending the dust grain population to larger sizes (e.g. WD01). However, ZDA model distributions with large dust grains composed of amorphous carbon or composite materials can also reproduce the average Milky Way extinction curve of  $R_V = 3.1$ .

Fig. 10 shows the extinction curves calculated from the best-fitting models in Sections 3.1, 3.2, and 5.2. We found that a 60/40

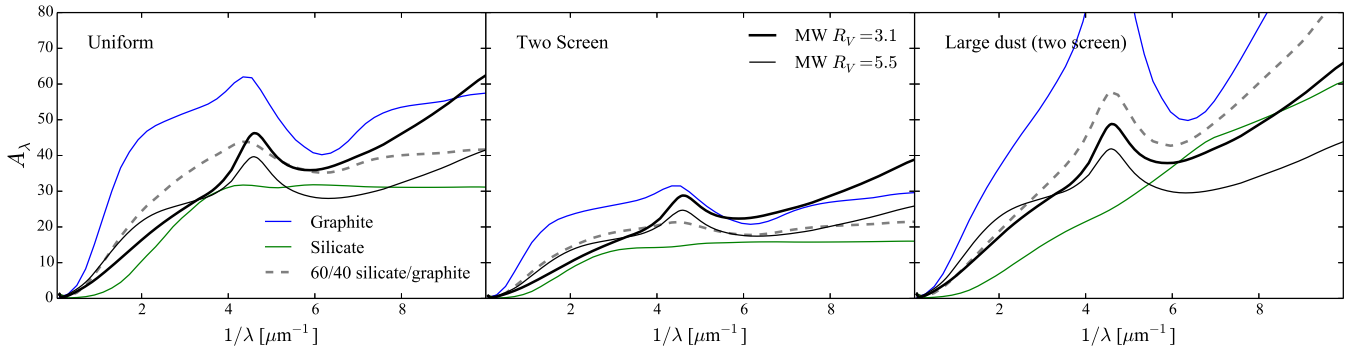


**Figure 10.** The extinction curves utilizing the best-fitting grain size distributions are shown for the uniform (left), two-screen (middle), and large grain (right) models for the X-ray scattering halo of Cyg X-3. The true extinction values must be somewhere between that of pure graphite (blue) and silicate (green). The synthetic extinction curves of WD01 for  $R_V = 3.1$  and  $5.5$  Milky Way dust are shown for comparison. We use a 60 per cent silicate, 40 per cent graphite mix of grains (grey dashed line) to estimate the total  $A_V$  towards Cyg X-3 for each model.

mix of silicate/graphite grains with an MRN size distribution of  $p = 3.5$  and  $a_{\max} = 0.3$  roughly matches the synthetic  $R_V = 3.1$  extinction curve from WD01. We use this mixture as a guess for the total extinction towards Cyg X-3, because at this time we cannot constrain the composition of our dust grains from the dust scattering halo alone. The variation in total magnitude of extinction seen in Fig. 10 comes from the different dust masses (parametrized by  $N_H$ ) implied by the fits.

In the cases of the best-fitting uniform and two-screen models, the extinction curve in the optical band more closely resembles the  $R_V = 5.5$  curve. This is due mainly to the fact that the best-fitting walkers in the distribution both have shallower power laws ( $p < 3$ ) than the median values, putting greater weight towards large grains. The extinction curve calculated from the fit incorporating micron-sized grains more closely resembles the  $R_V = 3.1$  curve because the majority of the dust mass is in the population of MRN-type grains held fixed with the Perseus arm.

The continuum fit to the X-ray spectrum of Cyg X-3,  $N_H \sim 4 \times 10^{22} \text{ cm}^{-2}$ , implies a total extinction of  $A_V \sim 20$  using the relations of Predehl & Schmitt (1995) and Güver & Özel (2009). The curves shown in Fig. 10 are roughly consistent with this value, but it depends strongly on the relative abundance of dust types. The 60/40 mixture of silicate to graphite produces  $A_V = 22, 13$ , and 17 for the uniform, two-screen, and large dust models, respectively.

## 6 COMPARISON TO OTHER X-RAY SCATTERING HALO STUDIES

Predehl & Schmitt (1995, hereafter PS95) included Cyg X-3 in a study of X-ray scattering haloes visible with *ROSAT*. The halo around Cyg X-3, being 40 per cent as bright as the central point source, had the largest optical depth in the study. Since the *ROSAT* PSF is much broader, only the outer part of the halo ( $\alpha > 100$  arcsec) was visible, leading them to be more sensitive to dust close to the observer. Regardless, they got similar values for  $a_{\max}$  (0.20  $\mu\text{m}$ ) and  $p$  (3.8), which are consistent with our uniform fit.

The scattering halo of Cyg X-3 was also included in a broad study of high- and low-mass X-ray binaries (Xiang, Zhang & Yao 2005). Using ObsID 425, they extracted the halo image from the 1D projection of the halo data along the direction of the MEG arm (see also Yao et al. 2003). All of their binaries exhibited surface brightness profiles that are steep in the inner 5 arcsec (10 pixels) and less steep

in the outer regions. This led them to conclude that all of the objects in the study were embedded in molecular clouds, because all of the dust mass needed to be located very close to the X-ray sources. In the case of Cyg X-3, this required  $N_H \sim 4 \times 10^{22} \text{ cm}^{-2}$  within 100 pc of the HMXB. Our study does not resolve the scattering halo within 5 arcsec, but most of our two-screen fits do require a significant mass of dust within 1–2 kpc of Cyg X-3. It is also possible that the particularly indirect method they used to resolve the scattering halo led to a systematic error in the inner regions of the halo. We measure the scattering halo directly from the zeroth-order image of HETG TE-mode data instead.

Ling, Zhang & Tang (2009) performed an in depth cross-correlation timing analysis of Cyg X-3 to determine the spatial distribution of dust. They found that dust associated with Cyg OB2 could account for time lags in the  $\alpha > 65$  arcsec halo, but that only accounted for 7 per cent of the total dust along the line of sight. The remainder of the data was well fitted with uniformly distributed dust. We do not perform a uniform plus screen fit because the screen contribution would be similarly negligible.

Depending on the Cyg OB2 distance, Ling et al. (2009) measured 3.4, 7.2, and 9.3 kpc to Cyg X-3. We put rather strict priors on the screen positions to correspond to the Perseus and outer spiral arms of the Milky Way, because the scattering halo from MRN-type dust in the nearby Cyg OB2 cluster would not be contribute enough to the  $\alpha \leq 100$  arcsec scattering halo to substantially affect our fits. For the sake of thought experiment, associating Screen 1 with the Cyg OB2 cluster at  $1.4 \pm 0.08$  kpc (Rygl et al. 2012) requires Cyg X-3 to be  $2.5^{+0.6}_{-0.5}$  kpc away. If Screen 1 is associated with the Perseus arm  $5.6 \pm 0.5$  kpc away (fig. 1 of Reid et al. 2014), then our posterior distribution from Section 3.2 implies that Cyg X-3 is  $9.8^{+2.4}_{-2.1}$  kpc away, which is consistent with Predehl et al. (2000).

## 7 CONCLUSION

In the appendix, we present an analytic solution for the dust scattering halo intensity from a power-law distribution of grain sizes in the single scattering RG–Drude regime. The solutions are in the form of erf and incomplete gamma functions, which are included in many common software packages such as Scientific PYTHON and MATHEMATICA. This allows for a probabilistic approach to fitting the data, which required computing  $\sim 10^5$  haloes for each of our dust



distribution models. The Bayesian approach is powerful because it allows us to explore and constrain the degeneracies that exist between dust grain size, power-law slope, and spatial distribution that produce scattering halo surface brightness profiles. The Bayesian analysis also allowed us to incorporate and quantify prior knowledge about the relative position of two dusty foreground screens.

We take this approach to analyse one of the brightest dust scattering haloes available in the *Chandra* archive, that associated with Cyg X-3. We find that a uniform distribution of dust along the line-of-sight fits the scattering halo profile for the region  $\alpha < 100$  arcsec. This suggests an MRN-type grain size distribution with a slightly smaller grain size cut-off than typically assumed,  $a_{\max} = 0.18 \pm 0.03 \mu\text{m}$ . The scattering halo can also be fitted with two infinitesimally thin dust screens placed in the foreground of Cyg X-3. About 80 per cent of the dust would be located about half-way along the sight line and is most likely associated with the Perseus spiral arm of the Milky Way. The remaining 20 per cent of the dust would have to be within 1 kpc of Cyg X-3, contributing most to the inner portion ( $r < 15$  pixels) of the scattering halo. The grain size distribution suggested by the two-screen fit has a similar cut-off to the uniform model ( $a_{\max} = 0.17^{+0.06}_{-0.04} \mu\text{m}$ ). Our results are consistent with other published conclusions regarding the distance to Cyg X-3 and the dust grain distribution along its sight line.

The fact that a power-law distribution of dust can well describe the shape of the 4–6 keV scattering halo attests to the survival of the MRN model, which has a noteworthy ability to describe Milky Way dust *on average*. This is surprising when we consider the variety of interstellar environments expected along the Cyg X-3 sight line, which includes young stellar clusters and molecular material in addition to the diffuse ISM. However, when we look at the broad-band energy resolved scattering haloes from 1 to 6 keV, the power-law distribution of dust grains fails due to the shortcomings of the RG–Drude approximation, the dust optical constants used, or both. The nature of the resolved soft energy  $E \lesssim 2.5$  keV scattering haloes, which are much dimmer than expected when extrapolating from the 4–6 keV fits, might be explained by the reduced scattering efficiency of soft energy X-rays by micron-sized grains. The molecular regions, foreground Bok globule, extinction properties, and evolved nature of many Cyg OB2 cluster members in the angular vicinity of Cyg X-3 suggest that this sight line might host dust grains of larger size or different composition than those in the diffuse ISM. However, we are unable to resolve this issue in the single scattering RG–Drude regime.

Finally, we would like to point out from the literature that all current interstellar grain models do not fit observed X-ray scattering haloes with  $\chi^2 < 2$ –5 (e.g. Smith et al. 2006; Valencic & Smith 2008), unless a significant number of free parameters are employed by incorporating multiple dust clumps in the ISM spatial distribution, as in this work and others (e.g. Valencic et al. 2009; Xiang et al. 2011). Since the RG–Drude approximation is strongly sensitive to dust grain size, it generally probes the upper limit of more complicated grain size distributions such as WD01 and ZDA. Our approach attempts to derive the grain size upper limit from the data. In the future, exponential decay around the grain size cut-off, dual power laws, or other parametrized distributions should be implemented in order to contribute to, not just test, our current understanding of grain size distributions and growth.

This work also presents resolved X-ray scattering haloes over a wider energy band than typically covered in the literature. Fits utilizing the RG–Drude approximation and single scattering regime differ significantly when applied to  $E \lesssim 2.5$  keV as opposed to those applied to higher energy bins, where the approximations are more

appropriate. We encourage future works treating dust scattering along optically thick  $N_{\text{H}} \gtrsim 10^{22} \text{ cm}^{-2}$  sight lines to examine  $E \gtrsim 2.5$  keV scattering. We also suggest that future researchers use the Mie scattering cross-section for  $E \lesssim 2.5$  keV scattering haloes from optically thick sight lines.

## ACKNOWLEDGEMENTS

The PYTHON code used to model the scattering haloes and extinction curves is available online at <http://github.com/eblur/dust> (Corrales 2015). This research has made use of the SIMBAD data base, operated at CDS, Strasbourg, France. This work was supported in part by NASA Headquarters under the NASA Earth and Space Science Fellowship Program, grant NNX11AO09H.

We thank Michael McCollough, R. K. Smith, L. Valencic, D. Foreman-Mackey, Herman L. Marshall, John Davis, John Houck, and the entire CXC staff at MIT for useful discussion and calibration advice.

## REFERENCES

- Andersen M., Steinacker J., Thi W.-F., Pagani L., Bacmann A., Paladini R., 2013, *A&A*, 559, A60
- Bohren C. F., Huffman D. R., 1983, *Absorption and Scattering of Light by Small Particles*. Wiley, New York
- Brinkman A., Parsignault D., Giacconi R., Gursky H., Kellogg E., Schreier E., Tananbaum H., 1972, *IAU Circ.*, 2446, 1
- Canizares C. R. et al., 2005, *PASP*, 117, 1144
- Cardelli J. A., Clayton G. C., Mathis J. S., 1989, *ApJ*, 345, 245
- Comerón F. et al., 2002, *A&A*, 389, 874
- Corrales L., 2015, *Astrophysics Source Code Library*, record ascl:1503.005
- Dame T. M., Hartmann D., Thaddeus P., 2001, *ApJ*, 547, 792
- de Vries B. L., Maaskant K. M., Min M., Lombaert R., Waters L. B. F. M., Blommaert J. A. D. L., 2015, *A&A*, 576, A98
- Dickey J. M., 1983, *ApJ*, 273, L71
- Draine B. T., 2003a, *ARA&A*, 41, 241
- Draine B. T., 2003b, *ApJ*, 598, 1026
- Draine B. T., 2011, *Physics of the Interstellar and Intergalactic Medium*. Princeton Univ. Press, Princeton, NJ
- Draine B. T., Li A., 2007, *ApJ*, 657, 810
- Foreman-Mackey D., Hogg D. W., Lang D., Goodman J., 2013, *PASP*, 125, 306
- Gaetz T. J., Edgar R. J., Jerius D. H., Zhao P., Smith R. K., 2004, in Flanagan K. A., Siegmund O. H. W., eds, *Proc. SPIE Conf. Ser. Vol. 5165, X-Ray and Gamma-Ray Instrumentation for Astronomy XIII*. SPIE, Bellingham, p. 411–422.
- Gaetz T. J., 2010, *Analysis of the Chandra On-Orbit PSF Wings*. Available at: [http://cxc.harvard.edu/cal/Hrma/rsrc/Publish/Optics/PSFWings/wing\\_analysis\\_rev1b.pdf](http://cxc.harvard.edu/cal/Hrma/rsrc/Publish/Optics/PSFWings/wing_analysis_rev1b.pdf)
- Gierliński M., Zdziarski A. A., Poutanen J., Coppi P. S., Ebisawa K., Johnson W. N., 1999, *MNRAS*, 309, 496
- Güver T., Özel F., 2009, *MNRAS*, 400, 2050
- Hanke M., Wilms J., Nowak M. A., Pottschmidt K., Schulz N. S., Lee J. C., 2009, *ApJ*, 690, 330
- Juett A. M., Schulz N. S., Chakrabarty D., 2004, *ApJ*, 612, 308
- Juett A. M., Schulz N. S., Chakrabarty D., Gorczyca T. W., 2006, *ApJ*, 648, 1066
- Kalberla P. M. W., Burton W. B., Hartmann D., Arnal E. M., Bajaja E., Morras R., Pöppel W. G. L., 2005, *A&A*, 440, 775
- Knödseder J., 2003, in van der Hucht K., Herrero A., Esteban C., eds, *Proc. IAU Symp. 212, A Massive Star Odyssey: From Main Sequence to Supernova*. Astron. Soc. Pac., San Francisco, p. 505
- Li A., Greenberg J. M., 1997, *A&A*, 323, 566
- Ling Z., Zhang S. N., Tang S., 2009, *ApJ*, 695, 1111
- McCollough M. L., Smith R. K., Valencic L. A., 2013, *ApJ*, 762, 2
- Mathis J. S., Lee C.-W., 1991, *ApJ*, 376, 490

- Mathis J. S., Rimpl W., Nordsieck K. H., 1977, *ApJ*, 217, 425  
 Mauche C. W., Gorenstein P., 1986, *ApJ*, 302, 371  
 Min M., Hovenier J. W., de Koter A., 2003, *A&A*, 404, 35  
 Nowak M. A., Juett A., Homan J., Yao Y., Wilms J., Schulz N. S., Canizares C. R., 2008, *ApJ*, 689, 1199  
 Overbeck J. W., 1965, *ApJ*, 141, 864  
 Predehl P., Schmitt J. H. M. M., 1995, *A&A*, 293, 889  
 Predehl P., Burwitz V., Paerels F., Trümper J., 2000, *A&A*, 357, L25  
 Reid M. J. et al., 2014, *ApJ*, 783, 130  
 Rolf D. P., 1983, *Nature*, 302, 46  
 Russeil D., 2003, *A&A*, 397, 133  
 Rygl K. L. J. et al., 2012, *A&A*, 539, A79  
 Schlegel D. J., Finkbeiner D. P., Davis M., 1998, *ApJ*, 500, 525  
 Smith R. K., 2008, *ApJ*, 681, 343  
 Smith R. K., Dwek E., 1998, *ApJ*, 503, 831  
 Smith R. K., Edgar R. J., Shafer R. A., 2002, *ApJ*, 581, 562  
 Smith R. K., Dame T. M., Costantini E., Predehl P., 2006, *ApJ*, 648, 452  
 Steinacker J., Pagani L., Bacmann A., Guieu S., 2010, *A&A*, 511, A9  
 Szostek A., Zdziarski A. A., McCollough M. L., 2008, *MNRAS*, 388, 1001  
 Tiengo A. et al., 2010, *ApJ*, 710, 227  
 Trümper J., Schönfelder V., 1973, *A&A*, 25, 445  
 Valencic L. A., Smith R. K., 2008, *ApJ*, 672, 984  
 Valencic L. A., Smith R. K., Dwek E., Graessle D., Dame T. M., 2009, *ApJ*, 692, 502  
 Vaughan S. et al., 2006, *ApJ*, 639, 323  
 Wang S., Li A., Jiang B. W., 2014, *Planet. Space Sci.*, 100, 32  
 Weingartner J. C., Draine B. T., 2001, *ApJ*, 548, 296  
 Weisskopf M. C., Tananbaum H. D., Van Speybroeck L. P., O'Dell S. L., 2000, in Truemper J. E., Aschenbach B., eds, *Proc. SPIE Conf. Ser. Vol. 4012, X-Ray Optics, Instruments, and Missions III*. SPIE, Bellingham, p. 2  
 Wilms J., Allen A., McCray R., 2000, *ApJ*, 542, 914  
 Witt A. N., Smith R. K., Dwek E., 2001, *ApJ*, 550, L201  
 Wright N. J., Drew J. E., Mohr-Smith M., 2015, *MNRAS*, 449, 741  
 Xiang J., Zhang S. N., Yao Y., 2005, *ApJ*, 628, 769  
 Xiang J., Lee J. C., Nowak M. A., Wilms J., 2011, *ApJ*, 738, 78  
 Yao Y., Zhang S. N., Zhang X., Feng Y., 2003, *ApJ*, 594, L43  
 Zdziarski A. A., Misra R., Gierliński M., 2010, *MNRAS*, 402, 767  
 Zubko V., Dwek E., Arendt R. G., 2004, *ApJS*, 152, 211

## APPENDIX A: SOLUTIONS FOR DUST SCATTERING FROM A POWER-LAW DISTRIBUTION OF GRAIN SIZES

The integral for the scattering halo intensity can be evaluated analytically under a few simple conditions. First, we assume that the grain size distribution is a power-law function of grain size

$$N_d \propto a^{-p}. \quad (\text{A1})$$

Secondly, we use the RG differential cross-section as described in the text (equation 2),

$$\frac{d\sigma}{d\Omega} \propto a^6 \exp\left(\frac{-\alpha^2 a^2}{2\tilde{\sigma}_0^2 x^2}\right), \quad (\text{A2})$$

where  $\tilde{\sigma}_0$  is the characteristic scattering angle for 1  $\mu\text{m}$  size grains, such that  $\tilde{\sigma}_0 = 1.04 \text{ arcmin } E_{\text{keV}}^{-1}$ .

Finally, we assume that the medium along the line of sight is optically thin to dust scattering. The single-scattering halo intensity, integrated over solid angle, is

$$\int I_h d\Omega = F_a \tau_{\text{sca}}. \quad (\text{A3})$$

For more information on second- or third-order scattering see Mathis & Lee (1991).

We can integrate equation (4) over solid angle to solve for one of our normalization factors. We will use  $A$  as a normalization constant that combines the dust grain size distribution and differential cross-section proportionalities described above,

$$F_a \tau_{\text{sca}} = F_a A \int a^{6-p} \int x^{-2} \xi(x) \times \int_0^\infty \exp\left(-\frac{\alpha^2 a^2}{2\tilde{\sigma}_0^2 x^2}\right) 2\pi\alpha d\alpha dx da. \quad (\text{A4})$$

Integrating over  $\alpha$  first will contribute an  $(x/a)^2$  term, and we will drop the  $\xi(x)$  term for now. This yields

$$A = \frac{\tau_{\text{sca}}}{2\pi\tilde{\sigma}_0^2 G_p(a, p)}, \quad (\text{A5})$$

where  $G_p$  is a constant:

$$G_p(a, p) \equiv \int_{a_{\min}}^{a_{\max}} a^{4-p} da. \quad (\text{A6})$$

Under the above simplifying notation, equation (4) becomes

$$I_h(\alpha) = \frac{F_a \tau_{\text{sca}}}{2\pi\tilde{\sigma}_0^2 G_p(a, p)} \times \int a^{6-p} \int x^{-2} \xi(x) \exp\left(-\frac{\alpha^2 a^2}{2\tilde{\sigma}_0^2 x^2}\right) dx da. \quad (\text{A7})$$

### A1 Screen case

In the case of an infinitesimally thin screen at position  $x_s$ , equation (A7) becomes

$$I_h(\alpha) = \frac{F_a}{x_s^2} \frac{\tau_{\text{sca}}}{2\pi\tilde{\sigma}_0^2 G_p(a, p)} \int a^{6-p} \exp\left(\frac{-\alpha^2 a^2}{2\tilde{\sigma}_0^2 x_s^2}\right) da \quad (\text{A8})$$

which produces the solution

$$I_h(\alpha) = \frac{F_a}{x_s^2} \frac{\tau_{\text{sca}}}{2\pi\tilde{\sigma}_0^2} \frac{G_s(a, p, \alpha, x_s)}{G_p(a, p)} \quad (\text{A9})$$

where

$$G_s(a, p, \alpha, x_s) \equiv -\frac{1}{2} \left[ \left( \frac{\alpha^2}{2\tilde{\sigma}_0^2 x_s^2} \right)^{\frac{p-7}{2}} \Gamma\left(\frac{7-p}{2}, \frac{\alpha^2 a^2}{2\tilde{\sigma}_0^2 x_s^2}\right) \right]_{a_{\min}}^{a_{\max}}. \quad (\text{A10})$$

### A2 Uniform case

In the case that the dust grains are uniformly distributed along the line of sight, equation (A7) becomes

$$I_h(\alpha) = \frac{F_a \tau_{\text{sca}}}{2\pi\tilde{\sigma}_0^2 G_p(a, p)} \times \int a^{6-p} \int x^{-2} \exp\left(-\frac{\alpha^2 a^2}{2\tilde{\sigma}_0^2 x^2}\right) dx da. \quad (\text{A11})$$

The  $x$  term of the integral evaluates to

$$\sqrt{\frac{\pi}{2}} \frac{\tilde{\sigma}_0}{\alpha a} \left[ 1 - \text{erf}\left(\frac{\alpha a}{\tilde{\sigma}_0 \sqrt{2}}\right) \right]. \quad (\text{A12})$$

Plugging this in, we get

$$I_h(\alpha) = \frac{F_a \tau_{\text{sca}}}{\alpha \tilde{\sigma}_0 \sqrt{8\pi} G_p(a, p)} \int a^{5-p} \left[ 1 - \text{erf} \left( \frac{\alpha a}{\tilde{\sigma}_0 \sqrt{2}} \right) \right] da. \quad (\text{A13})$$

The solution is

$$I_h = \frac{F_a}{\alpha \tilde{\sigma}_0} \frac{\tau_{\text{sca}}}{\sqrt{8\pi}} \frac{G_u(a, p, \alpha)}{G_p(a, p)}, \quad (\text{A14})$$

where

$$G_u(a, p, \alpha) \equiv \frac{1}{6-p} \left[ a^{6-p} \left( 1 - \text{erf} \left( \frac{\alpha a}{\tilde{\sigma}_0 \sqrt{2}} \right) \right) - \frac{1}{\sqrt{\pi}} \left( \frac{\alpha}{\tilde{\sigma}_0 \sqrt{2}} \right)^{p-6} \Gamma \left( \frac{7-p}{2}, \frac{\alpha^2 a^2}{2\tilde{\sigma}_0^2} \right) \right]_{a_{\min}}^{a_{\max}} \quad (\text{A15})$$

This paper has been typeset from a  $\text{\LaTeX}$  file prepared by the author.